

Nanoscale Advances

Accepted Manuscript

This article can be cited before page numbers have been issued, to do this please use: J. Liao, L. Zhou, Y. Wu, Z. Qian and P. Li, *Nanoscale Adv.*, 2024, DOI: 10.1039/D4NA00014E.



This is an Accepted Manuscript, which has been through the Royal Society of Chemistry peer review process and has been accepted for publication.

Accepted Manuscripts are published online shortly after acceptance, before technical editing, formatting and proof reading. Using this free service, authors can make their results available to the community, in citable form, before we publish the edited article. We will replace this Accepted Manuscript with the edited and formatted Advance Article as soon as it is available.

You can find more information about Accepted Manuscripts in the [Information for Authors](#).

Please note that technical editing may introduce minor changes to the text and/or graphics, which may alter content. The journal's standard [Terms & Conditions](#) and the [Ethical guidelines](#) still apply. In no event shall the Royal Society of Chemistry be held responsible for any errors or omissions in this Accepted Manuscript or any consequences arising from the use of any information it contains.

ARTICLE

Enhancing MRI imaging through high loading of superparamagnetic nanogels with high sensitivity to the tumor environment

Jinfeng Liao,^{§a} Liangyu Zhou,^{§b} Yongzhi Wu,^a Zhiyong Qian^c and Pei Li^{*b}Received 00th January 20xx,
Accepted 00th January 20xx

DOI: 10.1039/x0xx00000x

Tumors pose a significant threat to human health, and their occurrence and fatality rates are on the rise each year. Accurate tumor diagnosis is crucial in preventing untimely treatment and late-stage metastasis, thereby reducing mortality. To address this, we have developed a novel type of hybrid nanogels called $\gamma\text{-Fe}_2\text{O}_3\text{@PNIPAM/PAM/CTS}$, which contain iron oxide nanoparticles and poly(*N*-isopropyl acrylamide)/poly(acrylamide)/chitosan. The rationale for this study relies on the concept that thermosensitive PNIPAM has the ability to contract when exposed to the elevated temperature conditions found within tumors. This contraction leads to a dense clustering of the high-loading $\gamma\text{-Fe}_2\text{O}_3$ nanoparticles within the nanogel, thus greatly enhancing the capabilities of MRI imaging. Additionally, the amino groups in chitosan on the particle surface can be converted into ammonium salts under mildly acidic conditions, allowing for an increase in the charge of the nanogel specifically at the slightly acidic tumor site. Consequently, it promotes the phagocytosis of tumor cells and effectively enhances the accumulation and retention of nanogels at the tumor site. The synthesis of the hybrid nanogels involves a surfactant-free emulsion copolymerization process, where vinyl-modified $\gamma\text{-Fe}_2\text{O}_3$ superparamagnetic nanoparticles are copolymerized with the monomers in the presence of chitosan. We have optimized various reaction parameters to achieve a high loading content of the superparamagnetic nanoparticles, reaching up to 60%. The achieved r_2 value of $517.74 \text{ mM}^{-1}\text{s}^{-1}$ significantly surpasses that of the clinical imaging contrast agent Resovist (approximately $151 \text{ mM}^{-1}\text{s}^{-1}$). To assess the performance of these magnetic nanogels, we conducted experiments using Cal27 oral tumors and 4T1 breast tumors in animal models. The nanogels exhibited temperature- and pH-sensitivity, enabling magnetic targeting and enhancing diagnosis through MRI imaging. The results demonstrated the potential of these hybrid nanogels as contrast agents for magnetic targeting in biomedical applications.

1. Introduction

Tumors pose a significant and persistent risk to human well-being, with high fatality rates over the years due to the population aging and an increasing incidence of cancer among younger people^{1, 2}. Unfortunately, a major challenge lies in the delayed detection of tumors and the limitations of existing diagnostic techniques. As a result, diagnosis is often made at the late stage of tumors, when metastasis has already taken place or when tumors are difficult to control³. Therefore, there is a pressing need to enhance the accuracy and sensitivity of tumor diagnosis in order to achieve precise tumor diagnosis and improve the efficacy of tumor treatment.

Currently, clinical tumor diagnosis primarily relies on imaging techniques such as computed tomography (CT), positron emission tomography (PET), single photon emission computed tomography (SPECT), and magnetic resonance imaging (MRI)⁴⁻⁶. While PET and SPECT offer high sensitivity and penetration depth, they can be costly and raise concerns about radiation exposure for patients. In contrast, MRI diagnosis is more widely utilized in clinical settings due to its non-invasiveness, safety, high spatial resolution, and absence of tissue penetration limitations. In many clinical procedures, particularly for tumor detection and diagnosis, MRI contrast agents are employed to enhance device resolution and differentiate between diseased and normal tissues, thereby achieving accurate diagnostic outcomes⁷⁻⁹.

Clinical magnetic resonance contrast agents are primarily categorized as positive or negative contrast agents. Positive contrast agents rely on paramagnetic substances based on rhenium or manganese, which produce bright images in T1-weighted mode. Negative contrast agents, on the other hand, predominantly consist of superparamagnetic nanoparticles that generate dark images in T2-weighted mode¹⁰. The most commonly used MRI contrast agent in clinical practice is gadopentetate glucosamine (Gd-DTPA), known for its excellent thermodynamic stability and high relaxation rate¹¹. However, Gd-DTPA lacks specific distribution in the body. Moreover, in 2006, the US Food and Drug Administration (FDA) issued a statement highlighting the potential risk of renal systemic fibrosis

^a State Key Laboratory of Oral Diseases, National Center for Stomatology, National Clinical Research Center for Oral Diseases, West China Hospital of Stomatology, Sichuan University, Chengdu 610041, Sichuan, P. R. China.

^b Department of Applied Biology and Chemical Technology, The Hong Kong Polytechnic University, Hung Hom, Kowloon, Hong Kong, P. R. China.

^c State Key Laboratory of Biotherapy and Cancer Center, West China Hospital, Sichuan University, Chengdu 610041, Sichuan, P. R. China.

[§] Jinfeng Liao and Liangyu Zhou contribute equally to this work.

*Corresponding author: Pei Li, The Hong Kong Polytechnic University, E-mail: pei.li@polyu.edu.cn

†Electronic Supplementary Information (ESI) available: [details of any supplementary information available should be included here]. See DOI: 10.1039/x0xx00000x



associated with long-term use of Gd-DTPA contrast agent in patients with renal insufficiency or transplantation, thereby limiting its applications¹².

In comparison to paramagnetic substances-based positive contrast agents (rhenium or manganese), iron oxide-based negative contrast agents, particularly superparamagnetic iron oxide nanoparticles, have gained significant attention as a new generation of negative magnetic resonance contrast agents. These MRI contrast agents offer advantages such as excellent biocompatibility, high thermal stability, high relaxation rate, controllable size, good dispersibility, and easy surface functionalization¹³⁻¹⁵. Various iron oxide-based magnetic resonance contrast agents have already found utility in clinical practice. For instance, Ferumoxide is primarily used for liver and spleen imaging, while Ferruglose is employed in angiography and tumor microvessel detection.

Recently, magnetic nanoparticles have emerged as highly promising nanomaterials for enhancing tumor MRI imaging, magnetic targeting, and tumor hyperthermia¹⁶⁻²⁰. The effectiveness of MRI imaging induced by magnetic nanoparticles is influenced by various factors, including particle size, morphology, chemical composition, surface modification, and nanoparticle aggregation²¹⁻²⁵. Extensive research efforts have been devoted to increasing the T2 value of magnetic nanoparticles to improve MRI imaging. For instance, adjusting the particle size of iron oxide has enabled the development of superparamagnetic nanoparticles with both T1 and T2 imaging capabilities²⁶. Additionally, hybrid iron oxide nanoparticles incorporating manganese have been fabricated to achieve higher relaxation values²⁷. Furthermore, the T2 value can be significantly enhanced by achieving high loading or concentration of magnetic nanoparticles in the tumor region²⁸. Therefore, it is highly desirable to employ magnetic nanoparticles with a high magnetic moment and saturation magnetization, as they exhibit rapid response to an external magnetic field. However, the strong magnetic attraction between magnetosome particles can lead to aggregation and precipitation in water and biological fluid environments. Thus, the preparation of magnetic particles with a high loading of superparamagnetic nanoparticles and good particle stability remains a challenge.

Our approach to address the above-mentioned challenge is to form magnetic nanogels. The nanogel particles have a high swelling capacity in water, which results in a particle density close to that of water. This high swelling capability enhances the stability of the magnetic nanoparticles within the nanogel, preventing their sedimentation or aggregation. This stability also ensures that the magnetic nanoparticles are uniformly dispersed within the nanogel matrix. Furthermore, we utilize temperature-sensitive polymers with a cloud point temperature (T_{cp}) close to the body temperature to ensure that the nanogel remains stable and expanded in normal physiological conditions. However, in hyperthermic tumor environments, the nanogel undergoes shrinkage, leading to aggregation of the magnetic nanoparticles within the nanogel, thus improving MRI imaging. Poly(*N*-isopropylacrylamide) (PNIPAM) is a well-known polymer that exhibits a reversible hydration-dehydration

transition in its aqueous solution, causing phase separation above 32 °C^{29, 30}. Studies have shown that copolymerization of *N*-isopropylacrylamide (NIPAM) with the hydrophilic molecule such as acrylamide (Am) can increase the cloud point temperature (T_{cp}) in water³¹. Acrylamide imparts hydrophilicity to the copolymer, thereby increasing its water solubility. This increased hydrophilicity affects the intermolecular interactions and hydrogen bonding between the copolymer and water molecules, leading to an increase in the T_{cp} of the copolymer in water. Therefore, the T_{cp} of the copolymer can be tuned by adjusting the composition of NIPAM and acrylamide in the copolymerization process. By increasing the T_{cp} of the copolymer to a temperature close to the physiological body temperature (37 °C), the copolymer becomes responsive to temperature changes in the body. This feature is desirable for applications such as MRI imaging, where the nanogel can remain stable at lower temperatures but undergo a phase transition and form compact structure at higher temperatures, thus facilitating the MRI imaging of the tumor.

In addition, the core-shell nanogel containing a water-soluble chitosan shell provides pH-sensitive property to the magnetic nanogel. Chitosan is a biocompatible and biodegradable polysaccharide derived from chitin, and it possesses pH-sensitive properties³². At the slightly acidic tumor site, the chitosan coating undergoes a pH-dependent transformation. The amino groups present in chitosan can be converted into ammonium salts due to the lower pH in the tumor microenvironment. This conversion leads to an increase in the nanoparticle's charge, making it more positively charged. This design strategy enables the particles to specifically respond to the acidic tumor microenvironment, enhancing their accumulation and retention at the tumor site³³⁻³⁶. Furthermore, having a water-soluble polymer on the particle surface improves the behaviour of particles in the bloodstream by enhancing stability, prolonging circulation time, improving biodistribution, and increasing biocompatibility. These advantages contribute to the overall efficacy and safety of the particles for MRI imaging. Therefore, the combination of MRI-enhanced imaging and responsive particles holds great promise for advancing tumor theranostics³⁷⁻³⁹.

In this study, we aim to develop a novel type of magnetic particles for accurate tumor diagnosis through MRI imaging. The designed particle encompasses several desirable characteristics: 1) High loading capacity of superparamagnetic nanoparticles and saturation magnetization with good particle stability. 2) Temperature sensitivity with a cloud point above the physiological temperature of 37 °C, enabling them to respond to temperature changes. 3) pH Responsiveness to specifically respond to the acidic tumor microenvironment, thus enhancing the cellular uptake within acidic milieu around tumor. 4) Good biocompatibility. To fulfil these requirements, we synthesized a magnetic nanogel, namely iron oxide/poly(*N*-isopropyl acrylamide)/poly(acrylamide)/chitosan (γ-Fe₂O₃@PNIPAM/PAm/CTS) using a surfactant-free emulsion copolymerization method. This involved combining vinyl-modified γ-Fe₂O₃ nanoparticles, water-soluble chitosan, *N*-isopropyl acrylamide, and acrylamide in the presence of a crosslinker through a step-wise



feeding process. The chemical crosslinking between the polymer and the magnetic nanoparticles enabled high loading while minimizing leakage of the iron oxide nanoparticles. Furthermore, the resulting $\gamma\text{-Fe}_2\text{O}_3\text{@PNIPAM/PAM/CTS}$ nanogels exhibited a three-dimensional structure with a porous network. These core-shell nanogels with water-soluble chitosan on the particle surface could absorb water, reaching a density similar to that of water, thereby ensuring good stability in an aqueous system, as well as in blood circulation. The performance of the temperature and pH-sensitive magnetic nanogels was assessed through MRI imaging using animal models with Cal27 oral and 4T1 breast tumors. Meanwhile, magnetic field was used at the tumor site for magnetic targeting imaging. The results demonstrated the potential of these hybrid nanogels as contrast agents for magnetic targeting and enhanced MRI imaging.

2. Materials and methods

2.1. Materials

The following chemicals including ferrous chloride tetrahydrate ($\text{FeCl}_2 \cdot 4\text{H}_2\text{O}$, Aldrich), anhydrous ferric chloride (FeCl_3 , Fluka), ammonia solution ($\text{NH}_3 \cdot \text{H}_2\text{O}$, concentration of 32 w/w%, VWR), nitric acid (HNO_3 , 65 w/w%, Merck), trisodium citrate dihydrate ($\text{Na}_3\text{C}_6\text{H}_5\text{O}_7 \cdot 2\text{H}_2\text{O}$, Riedel-de Haën), tetraethyl orthosilicate (TEOS, Sigma), 3-(trimethoxysilyl) propyl methacrylate (MPS, 98%, Sigma), chitosan (CTS, medium molecular weight, Aldrich), acetic acid solution (0.6 v/v%), hydrogen peroxide (H_2O_2 , 0.1 M); acrylamide (AM, 98.5%, Acros), and *N,N'*-methylenebis(acrylamide) (MBA, 97%, BDH Chemicals Ltd) were all used as received. *N*-isopropyl acrylamide powder (NIPAM, Tokyo Chemical industry Co. Ltd.) was purified through recrystallization in hexane before use. Deionized water (DI water) from Milli-Q Gradient System was used in all experiments.

Female Balb/c mice (6-8 weeks old) and nude female Balb/c mice (6-8 weeks old) were purchased from Beijing HFK Bioscience Co. Ltd, China. They were fed with water and standard laboratory chow. The animal housing area was maintained at 24 °C for 12 h in a light/dark cycle. All animal procedures complied with the guidelines of the Institutional Animal Care and Use Committee (Code number: WCHSIRB-D-2019-074) and were approved by the animal care and use committee of West China Hospital of Stomatology, Sichuan University, P. R. China.

2.2. Synthesis of vinyl-coated $\gamma\text{-Fe}_2\text{O}_3$ nanoparticles

The vinyl-coated $\gamma\text{-Fe}_2\text{O}_3$ nanoparticles ($\text{MPS-}\gamma\text{-Fe}_2\text{O}_3$) were first synthesized according to our previously established method⁴⁰. The procedure is described in detail in Supporting Information. The as-prepared $\text{MPS-}\gamma\text{-Fe}_2\text{O}_3$ nanoparticles were purified by dialysis and then dispersed in ethanol for subsequent use.

2.3. Synthesis of $\gamma\text{-Fe}_2\text{O}_3\text{@PNIPAM/CTS}$ nanogels

The $\gamma\text{-Fe}_2\text{O}_3\text{@PNIPAM/CTS}$ hybrid nanogels were synthesized by free-radical grafting and crosslinking polymerization of chitosan and NIPAM in aqueous solutions. The chitosan powder (0.5 g) was dissolved in 44 mL acetic acid (0.6 w/w %) under sonication and stirred at 300 rpm for 10 minutes. The purified $\text{MPS-}\gamma\text{-Fe}_2\text{O}_3$ solution (3.0 mL, 2.3 wt% in ethanol) was added to the chitosan solution dropwise. The mixture was then sonicated and stirred at 300 rpm for

30 min. The chitosan/ $\text{MPS-}\gamma\text{-Fe}_2\text{O}_3$ mixture was then transferred to a three-necked water-jacketed reaction flask equipped with a magnetic stirrer, a condenser, and a nitrogen inlet. The mixture was diluted with an acetic acid solution (46 g, 0.6 v/v %), followed by stirring at 360 rpm at 80 °C under nitrogen for 30 min. The aqueous solution of NIPAM (0.52 g) and MBA (0.0028 g) was prepared by dissolving them in 5 mL DI-water and purging solution with N_2 for 15 min at room temperature. The prepared monomer solution was then added into the reaction flask dropwise, followed by the addition of H_2O_2 solution (51 μL , 0.1 M). The reaction was allowed to react for 8 h at 80 °C under a nitrogen atmosphere.

2.4. Synthesis of $\gamma\text{-Fe}_2\text{O}_3\text{@PNIPAM/PAM/CTS}$ nanogels

Similar to procedure 2.3 except that the monomers were charged to the reaction mixture via a step-wise feeding method. An AM monomer (0.1228 g), which was pre-dissolved in 2 mL DI water and purged with N_2 for 15 min, was added into the three-necked water-jacketed reaction flask dropwise, followed by addition of 25 μL H_2O_2 solution (0.1 M). After reacting for 30 min, a NIPAM monomer solution, which was prepared by dissolving 0.1228 g purified NIPAM powder and 0.0028 g MBA in 3 mL DI-water and purged with N_2 for 15 min, was added into the flask dropwise, followed by addition of another 26 μL H_2O_2 solution (0.1 M). The reaction was allowed to react for 8 h at 80 °C under a nitrogen atmosphere. The product was purified by centrifugation three times with DI water. Monomer conversion was calculated gravimetrically according to the following equation:

$$C_m\% = \frac{W_p \times C_s - W_{\text{CTS}} - W_c}{W_m} \times 100\%$$

Here, C_m is the monomer conversion; W_p is the weight of product; W_{CTS} is the weight of chitosan; W_c is the weight of crosslinker; W_m is the weight monomer added in.

2.5. Characterization of magnetic nanogels

2.5.1. Structure analysis and morphology observation

Chemical structures were identified using a Nicolet Avatar 360 FTIR spectrophotometer. Morphologies of the hybrid particles were observed with transmission electron microscopy (TEM) (JEOL, JEM-2011) at an acceleration voltage of 100 kV. The samples were prepared by wetting a carbon-coated grid with a small drop of dilute dispersion (70 to 100 ppm), followed by drying the solution at room temperature.

2.5.2. Particle size and surface charges

The particle size and size distribution of samples were measured on a Malvern™ Zetasizer Nano S9 based on the electrophoretic dynamic light scattering (DLS) at 658 nm wavelength and 30 mV with the scattering angle at 174°. The concentration of the samples dispersed in DI water was adjusted to around 20 ppm with a pH between 5 and 6. The surface charges of the samples were also measured by the Malvern™ Zetasizer Nano S9 with a scattering angle at 173°. The concentration of samples was diluted to 20 ppm.

2.5.3. Temperature sensitivity of the nanogels

The percentage of shrinking volume was calculated according to the following equation where R_t is the hydrodynamic particle size at t °C, and R_0 is the particle size at a specific temperature (25 or 37 °C).



The shrinking volume was calculated according to the following equation:

$$\text{Shrinking Volume \%} = \left(1 - \frac{R_t^3}{R_0^3}\right) \times 100\%$$

2.5.4. Determination of encapsulated iron oxide content

The loading content of iron oxide nanoparticles was determined by thermogravimetric analysis (TGA) using a Thermogravimetric analyzer (Mettler Toledo™ TGA/DSC3+). The dried sample (~5 mg) was placed in a ceramic holder, followed by heating from 25 to 900 °C at a heating rate of 10 °C/min under 20 mL/min nitrogen flow. The iron oxide content was calculated based on the following equation:

$$\text{Encapsulated iron oxide (\%)} = \frac{\text{sample weight at } 800\text{ }^{\circ}\text{C}}{\text{sample weight at } 25\text{ }^{\circ}\text{C}} \times 100\%$$

2.5.5. Vibrating sample magnetometer (VSM) analysis

The saturation magnetization of the $\gamma\text{-Fe}_2\text{O}_3\text{@PNIPAM/PAm/CTS}$ nanogels was measured by a Vibrating Sample Magnetometer (VSM) (PPMS model 6000 Quantum Design, San Diego, USA). The measurement was conducted at room temperature under an external magnetic field H ranging from 0 to ± 300000 Oe.

2.6. In vitro cytotoxicity

In vitro cytotoxicity of the $\gamma\text{-Fe}_2\text{O}_3\text{@PNIPAM/PAm/CTS}$ nanogels was investigated using mouse embryonic fibroblast (3T3) and CAL-27 cells (human tongue squamous carcinoma cell line). Cells were seeded into a 96-well plate (5×10^3 cells/well, 100 μL), followed by incubating under 37 °C for 24 h. Subsequently, the cells were treated with $\gamma\text{-Fe}_2\text{O}_3\text{@PNIPAM/PAm/CTS}$ nanogels of different concentrations ranging from 1.58 to 200 $\mu\text{g/mL}$. After incubation for 24 h, the cells were washed with PBS three times, and the cell viability was determined based on the absorbance of cell counting kit-8 (CCK-8) at 450 nm.

2.7. Cell uptake study

Cell uptake of $\gamma\text{-Fe}_2\text{O}_3\text{@PNIPAM/PAm/CTS}$ nanogels was studied using Cal27 oral tumor cells. The cells were rinsed with PBS when the confluence reached 80%. 50 $\mu\text{g/mL}$ nanogels were then incubated with cells at 37 °C for 2 h, according to the literature studies.^{41, 42} The medium pH was set at either 7.40 (control) or 6.86. Then the cells were gently washed with PBS to remove free nanogels and fixed with 4% paraformaldehyde. The magnetic nanogels taken by the cells were stained with Prussian blue and cells were stained with nuclear fast red. The cell images were recorded by an inverted fluorescence microscope (Leica, Germany).

2.8. The hemolysis study

The hemolysis study was conducted using a New Zealand white rabbit, which was anesthetized by pentobarbital sodium. The whole blood was drawn by an injection syringe from the heart of the rabbit. The blood was stirred by a glass rod in a beaker for 10 minutes to get rid of the fibrinogen. Subsequently, the blood was diluted with more than ten times the volume of normal saline. The diluted blood was centrifuged at 1000 r/min for 15 min until the supernatant was clear. The obtained erythrocytes were further diluted to 2% by normal saline for final use. $\gamma\text{-Fe}_2\text{O}_3\text{@PNIPAM/PAm/CTS}$ nanogels in different

concentrations were mixed with erythrocytes solution and incubated at 37 °C for 3 h. The positive and negative controls were water and normal saline, respectively. Finally, all samples were centrifuged and photographed. The morphology of red blood cells (RBCs), which had been incubated with saline or $\gamma\text{-Fe}_2\text{O}_3\text{@PNIPAM/PAm/CTS}$ nanogels, was analyzed by an inverted light microscope.

2.9. Systemic toxicity of $\gamma\text{-Fe}_2\text{O}_3\text{@PNIPAM/PAm/CTS}$ nanogels

Female BALB/c mice (3 mice/group) were administered with saline and $\gamma\text{-Fe}_2\text{O}_3\text{@PNIPAM/PAm/CTS}$ nanogels (30 mg/kg) through tail vein injection. After two-week, the blood and serum were collected and the blood hematology and biochemistry were evaluated using an automatic animal blood analyzer (Mindray BC-2800Vet) and blood cell analyzer (Roche Cobas 6000-C501), respectively. Furthermore, mice were sacrificed to obtain their major organs (heart, lung, liver, spleen, and kidney) for toxicity analysis. Tissues were fixed with 10% formalin, embedded in paraffin, sectioned, and stained with hematoxylin and eosin (H&E).

2.10. In vitro MRI test

The *in vitro* MRI analysis was performed by using different concentrations of nanogels to calculate the transverse relaxivity (r_2). Before MRI imaging, the nanogel samples were dispersed in an HNO_3/HCl solution (1:3). The iron concentrations were determined by an inductively coupled plasma-atomic emission spectroscopy (ICP-AES). MRI imaging was performed with a 7.0 T magnetic field using an MRI instrument (Bruker, German). The T_2 -weighted MRI images of the nanogels with various iron concentrations (0, 0.012, 0.024, 0.048, 0.072, 0.096, and 0.120 mM) were obtained by using a T_2 -weighted Fast-recovery fast spin-echo (FR-FSE) sequence. The parameters for T_2 relaxivity measurement were as follows: repetition time (TR) = 2500.0 ms, echo time (TE) = 33.0 ms, and field of view (FOV) = 3.50 cm. The r_2 value was calculated through the curve fitting of $1/T_2$ relaxation time against the iron concentration.

2.11. In vivo MRI imaging and magnetic targeting imaging

The Cal27 oral tumor-bearing nude mice were established in the armpit of mice. When the tumors grow to approximately 4 mm in diameter, the mice were administered with $\gamma\text{-Fe}_2\text{O}_3\text{@PNIPAM/PAm/CTS}$ nanogels (10 mg/kg, 0.2 mL). One group of mice was given a magnet adhered to the tumor site. The magnetic targeting strategy was not adopted to another group. Before injection, the T_2 -weighted MRI imaging was taken for control. At 1, 2, and 4 h post-injection, the MRI images obtained were compared for their magnetic targeting and non-targeting effects.

Meanwhile, *in vivo* MRI diagnosis was tested on Balb/c mice with 4T1 breast tumors. The mice were taken for imaging at 1 and 4 h. The parameters of the MRI *in vivo* test were as follows: TR = 2500.0 ms, TE = 33.0 ms, FOV = 3.00 cm, matrix = 256, slice thickness = 1 mm, flip-angle = 90°. The signal intensities were measured in the region of interest (ROI) of tumor tissue and the liver at different time intervals.

2.12. Statistical analysis

The statistical data were based on at least three independent repeated experiments, and Student's t-test was used for statistical comparisons. Statistical significance was considered when the p -value was less than 0.05.

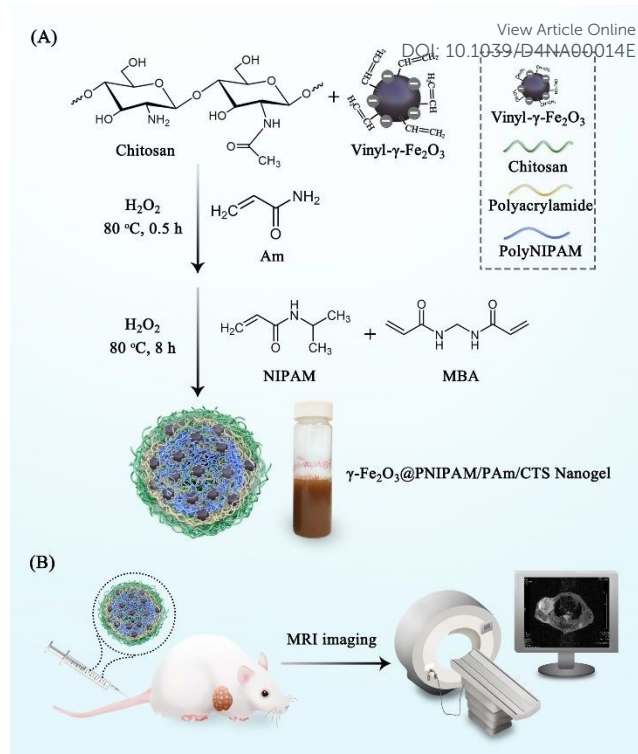


3. Results and Discussion

3.1. Synthesis of magnetic hybrid nanogels

The magnetic nanogels were synthesized using a previously established method for the preparation of γ -Fe₂O₃@poly(methyl methacrylate)/CTS particles⁴⁰. Scheme 1A illustrates reaction steps involved in the synthesis process. Initially, positively charged chitosan and negative charged vinyl-coated γ -Fe₂O₃ nanoparticles were mixed together in a weight ratio of 7.25 to 1, resulting in the formation of chitosan/ γ -Fe₂O₃ complexes. Subsequently, grafting and crosslinking copolymerization of *N*-isopropyl acrylamide, acrylamide, and *N*, *N*'-methylene bisacrylamide monomers were initiated using H₂O₂ as the initiator. Since the polymerization occurred at a temperature of 80 °C, which exceeded the phase transition temperature of PNIPAM, the growing chitosan/PNIPAM graft copolymer surpassed their water solubility. This led to the assembly of amphiphilic copolymers into particles, facilitating the copolymerization of NIPAM and vinyl-coated γ -Fe₂O₃ nanoparticles in the presence of MBA crosslinker. Consequently, crosslinked nanogel particles were formed. The prepared nanogels were then evaluated by injecting into tumor-bearing mice for MRI imaging (Scheme 1B).

We conducted a systematic study on the synthesis of magnetic nanogels, investigating the effects of various factors, including the addition method (one-shot or step-wise), reaction time (2, 8, 24 hours), chitosan to monomers weight ratio (3.46:1, 1.98:1, 0.82:1), and crosslinker concentration (2.3% and 5%). The results are shown in the section of Supporting Documents (Table S1 and Table S2). the optimal procedure and conditions for the synthesis process were that the graft copolymerization of acrylamide from the chitosan/ γ -Fe₂O₃ complexes occurred first, using H₂O₂ as the initiator. Subsequently, *N*-isopropyl acrylamide and *N*, *N*'-methylene bisacrylamide monomers were added. The optimal chitosan to monomer weight ratio was at approximately 2:1, with a 5% crosslinking. The polymerization took place at 80 °C for 8 hours, and the monomer conversion was above 70% as determined gravimetrically.



Scheme 1. (A) Illustration of the synthesis process of γ -Fe₂O₃@PNIPAM/PAM/CTS nanogels; (B) Nanogels were injected into tumor-bearing mice for MRI imaging.

3.2. Characterization of γ -Fe₂O₃@PNIPAM/PAM/CTS nanogels

TEM images in Figure 1A show the morphology of the γ -Fe₂O₃@PNIPAM/PAM/CTS nanogels, exhibiting a spherical shape with rough surface as well as sizes below 200 nm in the dry state. The cores and surfaces of the nanogels contain numerous γ -Fe₂O₃ nanoparticles (visible as dark dots). The stability of the nanogels was assessed by measuring their surface charge. The ζ -potential of the γ -Fe₂O₃@PNIPAM/PAM/CTS nanogels was determined to be +43.5 mV within a pH range of 5 to 6. The highly positive charge observed in acidic solutions indicates that chitosan effectively covers the nanogels' surface, resulting in good particle stability. To determine the loading content of magnetic nanoparticles in the nanogels, a thermogravimetric analysis (TGA) was conducted, and the results are presented in Figure 1B. The weight change before 110 °C can be attributed to the loss of residual solvent and water molecules. The PNIPAM molecules decomposed between 210 and 400 °C⁴³, while chitosan and polyacrylamide decomposed in the range of 200 to 500 °C^{44,45}. The remaining weight at 900 °C corresponds to the presence of the γ -Fe₂O₃ nanoparticles. The TGA analysis indicates that the iron oxide content within the hybrid nanogels was up to 60%. This high loading content suggests that our polymerization approach can efficiently encapsulate magnetic nanoparticles through copolymerization.



The chemical structures of the vinyl-modified magnetic nanoparticles (MPS- γ -Fe₂O₃) and γ -Fe₂O₃@PNIPAM/PAm/CTS nanogels were identified using an FT-IR spectrometer. Figure S1 in the Supporting Information displays characteristic peaks associated with MPS-coated iron oxides (red curve in the figure), including stretching vibrations of O-H (3417 cm⁻¹), C-H (2800-3000 cm⁻¹), C=O ester (1716 cm⁻¹), COO- (1634 cm⁻¹), Si-O (1100 cm⁻¹), and Fe-O (400-650 cm⁻¹). The spectrum of the γ -Fe₂O₃@PNIPAM/PAm/CTS nanogels (black curve in Figure S1) exhibits characteristic peaks that can be attributed to the presence of chitosan, PAm, PNIPAM, and iron oxide (γ -Fe₂O₃). These peaks include: Amine N-H and O-H stretching (3452 cm⁻¹), C-H stretching (2926 cm⁻¹), C=O ester (1716 cm⁻¹), C=O amide (1634 cm⁻¹), N-H bending (1557 cm⁻¹), C-N stretching, CH₂- and CH₃-bending vibrations (between 1350-1460 cm⁻¹), C-O stretching (1128 cm⁻¹), and Iron oxide (γ -Fe₂O₃, 637 cm⁻¹). Based on these peaks, it can be confirmed that the nanogels consist of chitosan, PAm, PNIPAM, and iron oxide components.

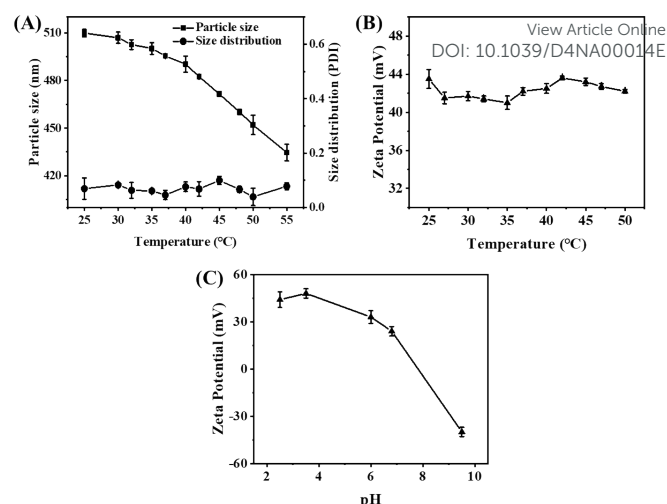


Figure 2 Effect of solution temperature between 25 and 55 °C on (A) hydrodynamic particle size, size distribution (PDI) and (B) zeta-Potential of γ -Fe₂O₃@PNIPAM/PAm/CTS nanogels; (C) The changes of zeta-potential of γ -Fe₂O₃@PNIPAM/PAm/CTS nanogels with the pH changing from acidic to alkaline condition.

The temperature sensitivity of the γ -Fe₂O₃@PNIPAM/PAm/CTS nanogels was investigated by measuring their sizes and size distribution (PDI) at various temperatures ranging from 25 to 55 °C. As depicted in Figure 2A, at 25 °C, the nanogels exhibited an average size of 509.9 nm (PDI = 0.06). As the solution temperature was increased to 40 °C, there was only a slight reduction in the nanogel sizes. However, upon further increasing the temperature above 40 °C, the nanogels underwent significant shrinkage. At 55 °C, the average size of the nanogels decreased to 434.6 nm (PDI = 0.08), which corresponds to a 38% reduction in size compared to their original size. This size reduction can be attributed to the phase transition of the PNIPAM chain, which undergoes a transition from a random coil to a collapsed state. Therefore, the phase transition of the γ -Fe₂O₃@PNIPAM/PAm/CTS hybrid particles was found to occur around 40 °C. Additionally, the PDI values between 25 and 55 °C remained relatively consistent, ranging from 0.050 to 0.078. These results indicate that the nanogels maintained excellent stability during the phase transition process.

Furthermore, the zeta-potential of magnetic nanogels remained above +40 mV as the solution temperature increased from 25 to 50 °C (Figure 2B). No noticeable agglomeration of the magnetic hybrid nanogels was observed in water. In Figure 2C, it can be observed that the zeta-potential of the γ -Fe₂O₃@PNIPAM/PAm/CTS nanogels shifted from negative to positive charge as the pH changed from alkaline to acidic conditions. This shift can be attributed to the conversion of the amino group of chitosan into quaternary ammonium ions under acidic environments. Therefore, the thermal-responsive and pH-sensitive properties of these magnetic nanogels make them highly desirable for stimuli-responsive drug release and sensing in tumor therapy.

3.3. In vitro cytotoxicity and pH-sensitivity to the tumor environment

The cytotoxicity of the magnetic nanogels was evaluated based on the study of cell viability. Figures 3A and 3B show less than 10% cell death in both 3T3 normal and Cal27 tumor cell lines when the

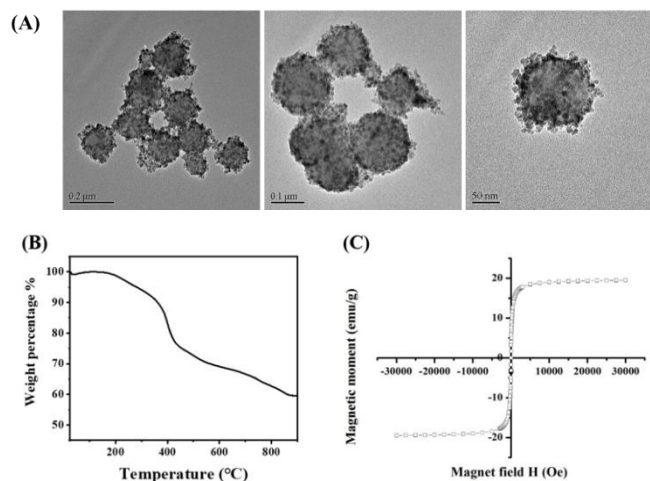


Figure 1 (A) The TEM images of γ -Fe₂O₃@PNIPAM/PAm/CTS nanogels; (B) The TGA thermogram of γ -Fe₂O₃@PNIPAM/PAm/CTS nanogels; (C) The magnetization loop of γ -Fe₂O₃@PNIPAM/PAm/CTS nanogels measured by VSM analysis.

The magnetic properties of the γ -Fe₂O₃@PNIPAM/PAm/CTS nanogels were assessed using Vibrating Sample Magnetometer (VSM) analysis. In Figure 1C, an S-shaped magnetization loop is observed, indicating the superparamagnetic nature of the nanogels. No hysteresis loops were observed, further confirming the superparamagnetic behaviour. The saturation magnetization (M_s) of the magnetic nanogels was measured to be 19.4 emu per gram of particles. By subtracting the weight of the polymer in the hybrid nanogels, the saturation magnetization of the encapsulated γ -Fe₂O₃ nanoparticles was calculated to be 98.1 emu per gram of maghemite. This value is higher than that of the citrate-coated γ -Fe₂O₃ nanoparticles (87.9 emu/g), indicating that the chemical modifications and polymerization processes did not alter the magnetic properties of the maghemite. The increase in saturation magnetization suggests an improvement in the magnetic performance of the hybrid nanogels, which could potentially enhance MRI imaging capabilities.



concentration of the nanogels increased to up to 200 $\mu\text{g/mL}$. The results indicate that the hybrid nanogels possess low cytotoxicity and good biocompatible for biological application.

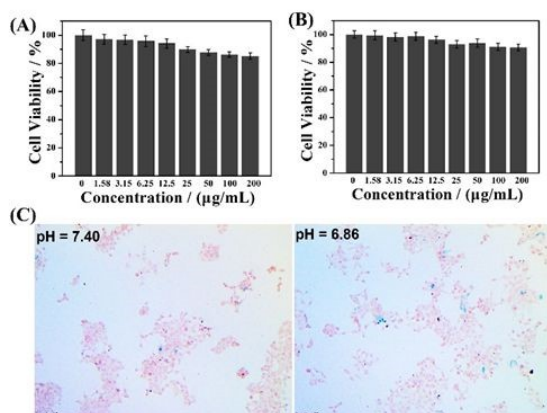


Figure 3 Cell viabilities of (A) 3T3 normal cells and (B) Cal27 cells treated with different concentrations of $\gamma\text{-Fe}_2\text{O}_3\text{@PNIPAM/PAm/CTS}$ nanogels. (C) Microscopy images of Cal27 tumor cells after incubation with 50 $\mu\text{g/mL}$ $\gamma\text{-Fe}_2\text{O}_3\text{@PNIPAM/PAm/CTS}$ nanogels for 2 h (Blue dots are the magnetic nanogels engrafted by tumor cells). Scale bar = 100 μm

The $\gamma\text{-Fe}_2\text{O}_3\text{@PNIPAM/PAm/CTS}$ nanogels developed in our study are expected to be pH-responsive under the acidic microenvironment of the tumor site. This is because the amino group of chitosan can be converted to quaternary ammonium ions under acidic conditions. The cationic nanogel surface is conducive to the phagocytosis of tumor cells, thus can effectively increase the accumulation and retention of the magnetic nanogels in tumor region and cells. Figure 3C compares *in vitro* intracellular uptake of the magnetic nanogels under different pH conditions with Prussian blue staining. The blue dots represent the magnetic nanogels stained with Prussian blue. The more blue dots there were, the more magnetic nanogels were taken up by tumor cells. Figure S2 shows comparison of the cellular uptake ratio which is calculated based on the cells engulfed nanoparticles divided by all cells. Results show that a higher number of nanogels was engrafted by the tumor cells at pH 6.86 than at pH 7.40, indicating the nanogels processing pH sensitivity to the tumor environment, which is promising for tumor theranostics.

3.4. The hemolysis study of $\gamma\text{-Fe}_2\text{O}_3\text{@PNIPAM/PAm/CTS}$ nanogels

The hemolytic analysis of $\gamma\text{-Fe}_2\text{O}_3\text{@PNIPAM/PAm/CTS}$ nanogels with concentrations ranging from 1 to 8 mg/mL was conducted. Figure S3A shows the supernatants of centrifuged erythrocytes samples. No significant difference was found when compared with the negative control group. The absorption of the supernatants was determined by a spectrophotometer at 540 nm. No hemolysis was observed even when the concentration of nanogels was up to 8 mg/mL. Moreover, morphology analysis of RBC as shown in Figure S3B indicated that no obvious changes or membrane destruction were observed with high concentration nanogel group. All the results suggest that the $\gamma\text{-Fe}_2\text{O}_3\text{@PNIPAM/PAm/CTS}$ nanogels possess good blood compatibility.

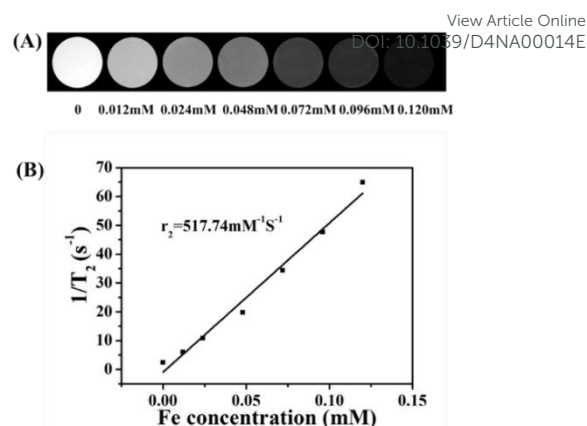


Figure 4 (A) *In vitro* T2-weighted MR images of $\gamma\text{-Fe}_2\text{O}_3\text{@PNIPAM/PAm/CTS}$ nanogels at different iron concentrations; (B) The plot of transverse relaxation rate versus iron concentration. The r_2 value (transverse relaxivity) was calculated based on the slope of the stimulated regression lines.

3.5. In vitro MRI imaging

Figure 4A shows *in vitro* T₂-weighted MR images of the $\gamma\text{-Fe}_2\text{O}_3\text{@PNIPAM/PAm/CTS}$ nanogels at different iron concentrations. Increasing concentrations from 0.012 to 0.120 mM resulted in darkening images. The transverse relaxivity (r_2), which is a measure of the change in the spin-spin relaxation rate (T_2^{-1}) per unit concentration⁴⁶, was determined by plotting the transverse relaxation rate versus iron concentration (Figure 4B). The r_2 value was then calculated based on the slope of the stimulated regression line to give $517.74 \text{ mM}^{-1} \text{ s}^{-1}$. This value is much higher than that of the clinical imaging contrast Resovist (r_2 value is $151 \text{ mM}^{-1} \text{ s}^{-1}$). Since the r_2 value is related to the particle size, morphology, surface modification and aggregation,^{21, 23, 25} The significant enhancement of the r_2 value may be attributed to the following three reasons: 1) the high loading capacity of our magnetic nanogel, 2) the aggregation of iron oxide nanoparticles encapsulated in the nanogels, 3) water penetration through swollen nanogels, thus enhancing the interaction between iron oxide nanoparticles and water molecules.

3.6. In vivo MRI imaging



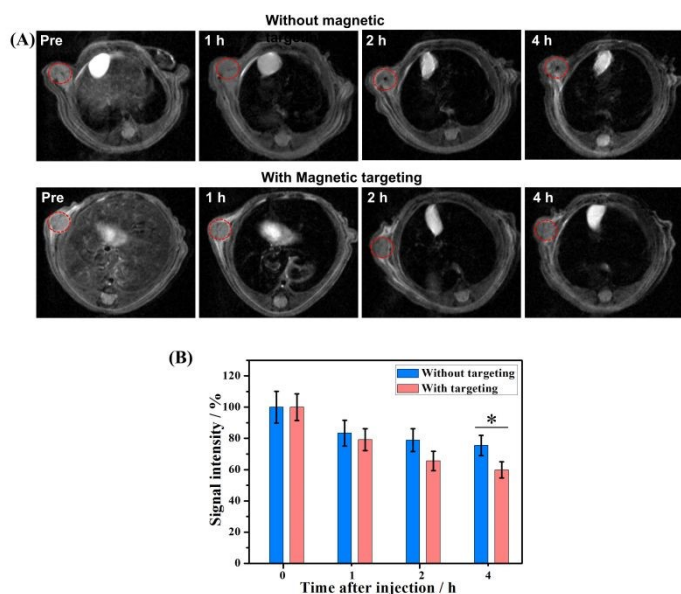


Figure 5 (A) In vivo T2-weighted MR images of nude mice bearing Cal27 oral tumor before and after injection with $\gamma\text{-Fe}_2\text{O}_3\text{@PNIPAM/Pam/CTS}$ nanogels at different time intervals. The tumor site of the mice treated with the magnet set as magnetic targeting group. (The red circles represent the tumor.) (B) Signal intensities of tumors in different groups before and after administration of magnetic nanogels. (* $P < 0.05$)

A high transverse relaxivity (r_2) value of $517.74 \text{ mM}^{-1}\text{s}^{-1}$ obtained from the *in vitro* MRI imaging prompted us to conduct the *in vivo* test on Cal27 tumor-bearing mice. Figure 5A shows that the T2-weighted images of the tumor treated with the $\gamma\text{-Fe}_2\text{O}_3\text{@PNIPAM/Pam/CTS}$ nanogels were darker than the pre-images at different time intervals. This is due to the fact that the iron oxide nanoparticles are commonly classified as T2, negative contrast agents. This classification is based on their ability to reduce the signal intensity in T2-weighted images, resulting in darker areas or negative contrast^{10, 47}. Figure 5B summarizes the results of signal intensities which were quantitatively analyzed by region of interest (ROI) within the tumor area. It was found that at 4 h post-injection, the magnetically targeted group has 1.28 times lower signal intensity than that of the non-targeting group. Therefore, the $\gamma\text{-Fe}_2\text{O}_3\text{@PNIPAM/Pam/CTS}$ nanogels not only can be potential MRI contrast reagents, but they can also be used for magnetic-enhanced applications because of their sensitivity towards tumor microenvironment and ability to accumulate at the tumor region under the guidance of magnetic targeting.

To further verify the enhancement of T₂-weighted MRI imaging using the magnetic nanogels, a breast tumor-bearing mice model was used and results are shown in Figure 6A, with the tumor region and liver marked with a red and yellow dashed circle, respectively. The darkness of these two parts appeared to increase with prolonged blood circulation time. For quantitative analysis, the signal intensity of the tumor decreased to 75.26% at 1 h, and to 70.43% at 4 h (Figure 6B). On the other hand, the signal intensity of the liver significantly reduced to 15.55% at 1 h, and to 14.88% at 4 h. These results suggest that the magnetic nanogels may be suitable for MRI imaging for both the tumor and liver. The enhanced contrast effect could remain for up to 4 h. Thus, the $\gamma\text{-Fe}_2\text{O}_3\text{@PNIPAM/Pam/CTS}$ nanogels may act as a long-lasting contrast agent for diagnosis of tumor and hepatic disease (especially hepatocellular carcinoma¹⁰).

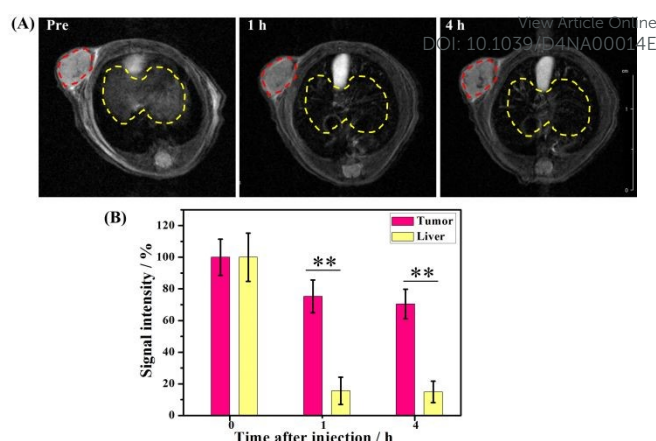


Figure 6 (A) In vivo T2-weighted MR images of mice bearing 4T1 breast tumor before and after administration of $\gamma\text{-Fe}_2\text{O}_3\text{@PNIPAM/Pam/CTS}$ nanogels at different time intervals (The red and yellow circles represent tumor and liver, respectively). (B) Comparison of signal intensities of tumor and liver before and after administration of $\gamma\text{-Fe}_2\text{O}_3\text{@PNIPAM/Pam/CTS}$ nanogels. (** $P < 0.01$)

3.7. Systemic toxicity of $\gamma\text{-Fe}_2\text{O}_3\text{@PNIPAM/Pam/CTS}$ nanogels

The biocompatibility studies of the $\gamma\text{-Fe}_2\text{O}_3\text{@PNIPAM/Pam/CTS}$ nanogels including blood analysis and tissue toxicity were conducted. Female BALB/c mice (3 mice/group) were administered with saline and magnetic nanogels (30 mg/kg) through tail vein injection. At two-week post-injection, the blood and serum were collected for blood hematology and biochemistry. No mortality, adverse effects, or body weight loss in the animals were found during the period. The hematology parameters and blood biochemistry results were normal and within the normal reference range (Figure S4). The results indicated that $\gamma\text{-Fe}_2\text{O}_3\text{@PNIPAM/Pam/CTS}$ nanogels were safe at the blood test level.

After blood analysis, the mice were sacrificed to obtain their major organs for histological analysis to assess the acute toxicity of $\gamma\text{-Fe}_2\text{O}_3\text{@PNIPAM/Pam/CTS}$ nanogels. Figure 7 shows that there is no significant damage in the tissues of the heart, kidney, liver, lung, or spleen. The *in vivo* results confirmed that the magnetic nanogels possessed no severe toxic effects on rodent animals.

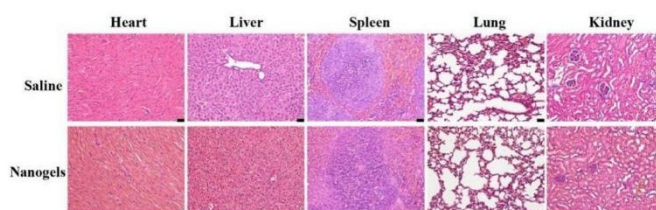


Figure 7 Histological images of the major organs of Balb/c mice after treatment for 2 weeks. The scale bars at the right corner are 20 μm .

Conclusions

We have successfully prepared magnetic nanogels ($\gamma\text{-Fe}_2\text{O}_3\text{@PNIPAM/Pam/CTS}$) containing high loading of superparamagnetic iron oxide nanoparticles as well as pH- and temperature-responsive polymer *via* the step-wise emulsion polymerization approaches. The magnetic nanogels contain high iron oxide loading of approximately 60% with good stability



in an aqueous system. They showed high magnetic saturation strength (r_2 value of $517.74 \text{ mM}^{-1}\text{s}^{-1}$) and were responsive to the tumor microenvironment, thus leading to enhanced *in vivo* MRI imaging. Systemic toxicity studies confirmed that the magnetic nanogels possessed no severe toxic effects on rodent animals. Our results demonstrated that the magnetic nanogels constructed in this study are promising contrast agents for magnetic targeting with long-lasting and enhanced MRI imaging, thus providing safe and improved contrast agents to the field of tumor diagnosis.

Author contributions

Jinfeng Liao: writing – original draft, writing – review & editing, conceptualization, Methods & methodology, formal analysis, investigation, data curation and funding acquisition. Liangyu Zhou: writing – original draft, writing – review & editing, Methods & methodology, formal analysis, and data curation. Yongzhi Wu: data curation. Zhiyong Qian: writing – review & editing. Pei Li: writing – manuscript & editing, conceptualization, supervision, project administration, funding acquisition. All authors have read and agreed to the published version of the manuscript.

Conflicts of interest

The authors declare no conflict of interest.

Acknowledgements

This work was financially supported by the Chengdu International Science and Technology Cooperation Project (2020-GH02-00048-HZ), the National Natural Science Foundation of China (32171354), NSFC/RGC Joint Research Scheme (N_PolyU533/14) and PolyU Lo Ka Chung Centre for Natural Anti-Cancer Drug Development.

References

1. R. L. Siegel, K. D. Miller and A. Jemal, *CA: a cancer journal for clinicians*, 2019, **69**, 7-34.
2. J. Ferlay, E. Steliarova-Foucher, J. Lortet-Tieulent, S. Rosso, J.-W. W. Coebergh, H. Comber, D. Forman and F. Bray, *European journal of cancer*, 2013, **49**, 1374-1403.
3. N. Riggi, M. Aguet and I. Stamenkovic, *Annual Review of Pathology: Mechanisms of Disease*, 2018, **13**, 117-140.
4. T. T. Wheeler, P. Cao, M. D. Ghouri, T. Ji, G. Nie and Y. Zhao, *Science China Chemistry*, 2022, **65**, 1498-1514.
5. N. Oriuchi, H. Endoh and K. Kaira, *International Journal of Molecular Sciences*, 2022, **23**, 9394.
6. D. Zhuang, H. Zhang, G. Hu and B. Guo, *Journal of Nanobiotechnology*, 2022, **20**, 1-21.
7. H. Chen, W. Zhang, G. Zhu, J. Xie and X. Chen, *Nature Reviews Materials*, 2017, **2**, 1-18.
8. G. Thomas, J. Boudon, L. Maurizi, M. Moreau, P. Walker, I. Séverin, A. Oudot, C. Goze, S. Poty and J.-M. Vrigneaud, *ACS omega*, 2019, **4**, 2637-2648.
9. P. Wang, W. Yang, S. Shen, C. Wu, L. Wen, Q. Cheng, B. Zhang and X. Wang, *ACS nano*, 2019, **13**, 11168-11180.
10. L. Chen, D. Niu, C. H. Lee, Y. Yao, K. Lui, K. M. Ho and P. Li, *Particle & Particle Systems Characterization*, 2016, **33**, 756-763.
11. B. Wu, S.-T. Lu, H. Yu, R.-F. Liao, H. Li, B. L. Zafitatisimo, Y.-S. Li, Y. Zhang, X.-L. Zhu and H.-G. Liu, *Biomaterials*, 2018, **159**, 37-47.
12. P. H. Kuo, E. Kanal, A. K. Abu-Alfa and S. E. Cowper, *Radiology*, 2007, **242**, 647-649.
13. B. T. Mai, S. Fernandes, P. B. Balakrishnan and T. Pellegrino, *Accounts of chemical research*, 2018, **51**, 999-1013.
14. B. Duan, D. Wang, H. Wu, P. Xu, P. Jiang, G. Xia, Z. Liu, H. Wang, Z. Guo and Q. Chen, *ACS Biomaterials Science & Engineering*, 2018, **4**, 3047-3054.
15. Y. Li, N. Wang, X. Huang, F. Li, T. P. Davis, R. Qiao and D. Ling, *ACS Applied Bio Materials*, 2019, **3**, 121-142.
16. M.-H. Chan, M.-R. Hsieh, R.-S. Liu, D.-H. Wei and M. Hsiao, *Chemistry of Materials*, 2019, **32**, 697-708.
17. S. Lu, X. Li, J. Zhang, C. Peng, M. Shen and X. Shi, *Advanced Science*, 2018, **5**, 1801612.
18. B. Muzzi, M. Albino, A. Gabbani, A. Omelyanchik, E. Kozenkova, M. Petrecca, C. Innocenti, E. Balica, A. Lavacchi and F. Scavone, *ACS Applied Materials & Interfaces*, 2022, **14**, 29087-29098.
19. M. Li, W. Bu, J. Ren, J. Li, L. Deng, M. Gao, X. Gao and P. Wang, *Theranostics*, 2018, **8**, 693.
20. K. Ma, S. Xu, T. Tao, J. Qian, Q. Cui, S. u. Rehman, X. Zhu, R. Chen, H. Zhao and C. Wang, *Proceedings of the National Academy of Sciences*, 2022, **119**, e2211228119.
21. Z. Zhou, L. Yang, J. Gao and X. Chen, *Advanced Materials*, 2019, **31**, 1804567.
22. L. Yang, Z. Wang, L. Ma, A. Li, J. Xin, R. Wei, H. Lin, R. Wang, Z. Chen and J. Gao, *ACS nano*, 2018, **12**, 4605-4614.
23. S. Ray, Z. Li, C.-H. Hsu, L.-P. Hwang, Y.-C. Lin, P.-T. Chou and Y.-Y. Lin, *Theranostics*, 2018, **8**, 6322.
24. Z. Wang, Y. Ju, Z. Ali, H. Yin, F. Sheng, J. Lin, B. Wang and Y. Hou, *Nature communications*, 2019, **10**, 4418.
25. N. Peng, X. Ding, Z. Wang, Y. Cheng, Z. Gong, X. Xu, X. Gao, Q. Cai, S. Huang and Y. Liu, *Carbohydrate polymers*, 2019, **204**, 32-41.
26. H. Du, Q. Wang, Z. Liang, Q. Li, F. Li and D. Ling, *Nanoscale*, 2022, **14**, 17483-17499.
27. G. Jiang, D. Fan, J. Tian, Z. Xiang and Q. Fang, *Advanced Healthcare Materials*, 2022, **11**, 2200841.
28. R. Wei, Z. Li, B. Kang, G. Fu, K. Zhang and M. Xue, *Nanoscale Advances*, 2023, **5**, 268-276.
29. F. D. Jochum and P. Theato, *Chemical Society Reviews*, 2013, **42**, 7468-7483.
30. L. Tang, L. Wang, X. Yang, Y. Feng, Y. Li and W. Feng, *Progress in Materials Science*, 2021, **115**, 100702.
31. Z. Shen, K. Terao, Y. Maki, T. Dobashi, G. Ma and T. Yamamoto, *Colloid and Polymer Science*, 2006, **284**, 1001-1007.
32. Q. Meng, S. Zhong, J. Wang, Y. Gao and X. Cui, *Carbohydrate Polymers*, 2023, **300**, 120265.
33. M. Ye, Y. Gao, M. Liang, W. Qiu, X. Ma, J. Xu, J. Hu, P. Xue, Y. Kang and Z. Xu, *Chinese Chemical Letters*, 2022, **33**, 4197-4202.
34. Y. Dai, C. Xu, X. Sun and X. Chen, *Chemical Society Reviews*, 2017, **46**, 3830-3852.
35. Y. Kato, S. Ozawa, C. Miyamoto, Y. Maehata, A. Suzuki, T. Maeda and Y. Baba, *Cancer cell international*, 2013, **13**, 1-8.



ARTICLE

Journal Name

36. W.-C. Huang, S.-H. Chen, W.-H. Chiang, C.-W. Huang, C.-L. Lo, C.-S. Chern and H.-C. Chiu, *Biomacromolecules*, 2016, **17**, 3883-3892.
37. X. Zhao, C.-X. Yang, L.-G. Chen and X.-P. Yan, *Nature communications*, 2017, **8**, 14998.
38. J. Liao, Y. Jia, Y. Wu, K. Shi, D. Yang, P. Li and Z. Qian, *Wiley Interdisciplinary Reviews: Nanomedicine and Nanobiotechnology*, 2020, **12**, e1581.
39. T. Wang, D. Wang, H. Yu, M. Wang, J. Liu, B. Feng, F. Zhou, Q. Yin, Z. Zhang and Y. Huang, *ACS nano*, 2016, **10**, 3496-3508.
40. K. M. Ho and P. Li, *Langmuir*, 2008, **24**, 1801-1807.
41. S. Zheng, J. Han, V. H. Le, J.-O. Park and S. Park, *Colloids and Surfaces B: Biointerfaces*, 2017, **154**, 104-114.
42. Q. Wu, Y. Lin, F. Wo, Y. Yuan, Q. Ouyang, J. Song, J. Qu and K. T. Yong, *Small*, 2017, **13**, 1701129.
43. Y.-Z. You, K. K. Kalebaila, S. L. Brock and D. Oupicky, *Chemistry of Materials*, 2008, **20**, 3354-3359.
44. M.-H. Yang, *Polymer testing*, 1998, **17**, 191-198.
45. Y. Du, M. Pei, Y. He, F. Yu, W. Guo and L. Wang, *PloS one*, 2014, **9**, e108647.
46. S. Balasubramaniam, S. Kayandan, Y.-N. Lin, D. F. Kelly, M. J. House, R. C. Woodward, T. G. St. Pierre, J. S. Riffle and R. M. Davis, *Langmuir*, 2014, **30**, 1580-1587.
47. J. Pellico, J. s. Ruiz-Cabello and F. Herranz, *ACS Applied Nano Materials*, 2023, **6**, 20523-20538.

View Article Online
DOI: 10.1039/D4NA00014E

